Proceedings of the Thirty-first (2021) International Ocean and Polar Engineering Conference **www.isope.org**
Rhodes, Greece, June 20 – 25, 2021

ISBN 978-1-880653-82-1; ISSN 1098-6189

Numerical Model of Wave-induced Coastal Hydrodynamic and Morphodynamic Processes

Georgios A. Leftheriotis
Department of Civil Engineering, University of Patras
Patras, Achaia, Greece

ABSTRACT

The aim of the present research is to present a numerical model for the simulation of wave hydrodynamics coupled with sediment transport and bed morphodynamics. The model is based on the formulation of three-dimensional (3D), large-eddy simulations with emphasis on the development of a morphological module under wave forcing. The numerical model has been effectively validated against numerical studies and laboratory measurements involving wave motion, sediment transport and morphodynamical evolution. Wave propagation and breaking are examined over an idealized beach with fixed bed of constant slope 1/15, as well as the corresponding suspended sediment transport. Moreover, the sediment transport mechanisms and the resulting morphological evolution of rippled beds were also examined under oscillatory flow conditions generated by non-breaking waves, with numerical results of ripple creation and growth presented.

KEY WORDS: Sediment transport; wave propagation; ripples; Navier-Stokes; immersed boundary; morphology evolution.

INTRODUCTION

The primary coastal process that causes shoreline erosion is the creation of strong bed shear stresses in the surf zone, which induce sediment motion and currents (cross-shore and long-shore) that carry the sediment offshore. This process continues until scouring phenomena take place and wave energy dissipation is in equilibrium with the eroded bed. A significant number of numerical models have been developed in recent years to simulate coastal processes. Dally & Dean (1984) were among the first to attempt the numerical modeling of coastal sediment transport, developing a mathematical model for coastline evolution. Depending on the wave and sediment characteristics, their model had the ability to generate both normal and storm-type beach profiles. Large-Eddy Simulation (LES) results combined with sediment transport over prototypical long-wave ripples, were presented by Zedler & Street, (2006). The authors concluded that the flow over such longer ripples is quite similar to the flow over vortex ripples. Marieu et al. (2008) developed a two-dimensional Reynolds-Averaged Navier-Stokes numerical model to simulate the development and morphological evolution of ripples, examining phenomena of ripple creation, development, merging, and annihilation. They also investigated the effect of the initial bed geometry on the morphological evolution, deducing that under the same flow characteristics the bed reaches the same equilibrium state regardless of the initial one. Kraft et al. (2011) simulated numerically the free-surface turbulent flow in a channel as well as the sediment transport over a rippled bed, using LES. In addition, they studied the morphological evolution of the rippled bed using the Level-Set method, and they used three different pickup relations for the sediment erosion. More recently, Jacobsen & Fredsøe (2014) analyzed the hydrodynamics of wave breaking combined with sediment transport over a fixed bottom of constant slope. They presented an empirical relationship for the phase lag between the breakpoint and the initiation of the setup, mentioning also that this phase lag determines the maximum values of the undertow and the bed shear stress. Leftheriotis & Dimas (2017) presented LES results of a three dimensional (3D) oscillatory turbulent flow, sediment transport and morphodynamics for the creation and development of ripples on a sandy bottom. It was shown that this model had the ability to capture ripple development, resulting in ripple lengths which were in agreement with those predicted by empirical equations. They concluded that under the same hydrodynamic forcing, the equilibrium state of the bed is the same, regardless of the initial bed form. Dimas & Leftheriotis (2019) conducted a parametric analysis for oscillatory flow and sediment transport over a fixed sandy bottom with ripples using the LES and 3D Immersed Boundary (IB) method. They found that the relative contribution of bed load versus suspended load on the total sediment load depends on both the mobility parameter and the non-dimensional sediment grain diameter. Finally, in their simulations the prediction of the vortex suspension parameter, P, was better than the phase-lag parameter, P_r, in distinguishing between bed and suspended load dominance. Dimas and Koutrouveli (2019) presented numerical results for wave propagation and spilling breaking over beach profiles of varying slopes using the IB and the Level-Set method with the bed profile and the free surface being immersed in a Cartesian grid. They found that the breaking depth and the wave height decreased as the beach slope increased or the surf-similarity parameter decreased. The generation of vorticity at the level of the free surface was mainly attributed to advection and secondarily to gravity.

Coastal processes like wave propagation and breaking, or flows over rough beds, are characterized by high turbulent motions with strong complexity due to their 3D, time-dependent, and nonlinear character (Argyropoulos and Markatos, 2015). Accurate numerical modelling of turbulence is quite demanding in terms of computational time and especially for cases of moderate to high Reynolds numbers.

The present research work is focused on the development of an advanced 3D hydrodynamic-morphological model, capable of utilizing High Performance Computing (HPC), to interpret at physical scale the wave hydrodynamics, sediment transport and morphodynamics that intertwine in coastal processes. For the flow equations, a fractional time-step scheme was used for the temporal discretization, while finite differences on a Cartesian grid were used for the spatial discretization. In the case of wave propagation, the evolution of the free surface was based on the Level-Set method (Sethian and Smereka 2003). The IB method was implemented for the imposition of fluid and sediment boundary conditions on the bed surfaces. The morphological evolution of the bed form was obtained by the numerical solution of the conservation of sediment mass equation, also known as the Exner equation. The numerical results are presented in two parts. In the first part, results of morphological evolution of sand ripples and sediment fluxes are presented in a relatively limited computational domain under oscillatory flow conditions due to non-breaking waves. In the second part, coupled results of wave propagation and breaking are presented in a larger computational domain of an ideal fixed coast of constant slope $\tan\beta$ = 1/15. The initial versions of the numerical model were first presented in Dimas & Leftheriotis (2019) for sediment transport over rippled beds and in Dimas & Koutrouveli (2019) for wave generation and breaking over fixed beaches of varying slopes.

FORMULATION

Hydrodynamics

Large eddy simulation (LES) is most commonly used for the numerical simulation of turbulent flows. In the LES approach, the flow structures are separated into the large and the small eddies. The small eddies are parametrized with the use of a subgrid scale (SGS) model, while the large eddies are explicitly solved. The governing flow equations are the continuity and the Navier-Stokes equations, which are presented below non-dimensionalized using the velocity amplitude U_o and the orbital motion amplitude a_o

$$\frac{\partial u_i}{\partial x_i} = 0 \tag{1}$$

$$\frac{\partial u_i}{\partial t} + \frac{\partial}{\partial x_j}\left(u_i u_j\right) = -\frac{\partial p}{\partial x_i} - \frac{\partial \tau_{ij}}{x_j} + \frac{1}{\mathrm{Re}}\frac{\partial^2 u_i}{\partial x_j \partial x_j} + f_i \tag{2}$$

In the above equations, x_i are the three Cartesian coordinates (x, y, z), u_i are the velocity components in the three directions (u, v, w), t is the time, p is the dynamic pressure and τ_{ij} are the SGS stresses. The SGS term has been modeled using the eddy-viscosity model, presented in Smagorinsky (1963). Re is the Reynolds number based on the orbital motion amplitude and f_i is a source term for the enforcement of non-slip boundary conditions on the immersed bed surface. The specific term is associated with the implementation of the IB method.

In the case of wave propagation, the combined water and air flow was modelled as one-fluid flow governed by the 3-D incompressible Navier-Stokes equations, appropriate to model flow in porous media (Koutrouveli and Dimas, 2020).

The Navier-Stokes equations were rendered dimensionless using the characteristic water depth d_0 of the incident waves and the gravitational acceleration g, meaning that the corresponding velocities were non-dimensionalized by $(g \cdot d_o)^{1/2}$. In the specific modified equations, the total pressure is considered, meaning the sum of the dynamic and the hydrostatic pressure.

The evolution of the free surface is based on the level-set method, following the advection equation, where φ is a signed distance function, defined to be equal to 1 at the level of the free surface.

$$\frac{\partial \varphi}{\partial t} + u_i \cdot \nabla \varphi = 0 \tag{3}$$

The 3D-IB method is implemented for the imposition of fluid flow and suspended sediment transport boundary conditions on the bed surface. The 3D approach of the IB method has been presented and described in detail in Dimas and Chalmoukis (2020). The spatial discretization of all equations is performed in a Cartesian grid, an advantage that is afforded by the use of the IB method. The temporal discretization for the Navier-Stokes equations is based on a time splitting projection method. Note that in the case of oscillatory flow over a rippled bed, the dynamic pressure in Eq. (2) is written as the sum $p = P + \delta P$ of the dynamic pressure P of the external oscillatory flow and the dynamic pressure correction δP due to the presence of the rippled bed surface. The dynamic pressure correction is computed by the numerical solution of a Poisson equation, and is subsequently used to obtain the final velocity field at each time step and simultaneously satisfy the continuity equation. Respectively, in the numerical simulations of wave propagation over a beach of constant slope, the final velocity field is computed after solving the Poisson equation for the total pressure.

Sediment Transport

In the present study, sediment transport comprises both bed load and suspended sediment. The bed load transport rate was computed using the semi-empirical formula in Engelund and Fredsøe (1976).

$$q_b = \begin{cases} \dfrac{10\pi}{6}\left[1+\left(\dfrac{\pi}{6}\dfrac{\mu_d}{|\theta|-|\theta_c|}\right)^4\right]^{-\frac{1}{4}}\left(\sqrt{|\theta|}-0.7\sqrt{|\theta_c|}\right) & , \quad \left(|\theta|>|\theta_c|\right) \\ 0 & , \quad \left(|\theta|\le|\theta_c|\right) \end{cases} \tag{4}$$

In the above equation, q_b is the bed load transport rate, μ_d is the dynamic friction coefficient, θ is the Shields parameter and θ_{co} is the corresponding critical Shields parameter, which is the criterion for incipient sediment motion, computed according to Van Rijn (1984). The evolution of sediment in suspension was modeled using a dimensionless advection-diffusion equation for the volumetric concentration, c, of the suspended sediment

$$\frac{\partial c}{\partial t} + u_j\frac{\partial c}{\partial x_j} - W_s\frac{\partial c}{\partial x_3} = -\frac{\partial \chi_j}{\partial x_j} + \frac{1}{\mathrm{Re}\cdot\sigma}\frac{\partial^2 c}{\partial x_j \partial x_j} + f_c \tag{5}$$

where W_s is the sediment settling velocity, χ_j is the SGS turbulent flux of sediment, σ is the Schmidt number, and f_c is a source term associated with the implementation of the IB method for the enforcement of the appropriate sediment concentration boundary condition on the bed surface. The SGS turbulent flux of sediment was modeled according to

$$\chi_j = \frac{\nu_{sgs}}{\sigma_t}\frac{\partial c}{\partial x_j} \tag{6}$$

where v_{sgs} is the non-dimensional SGS eddy-viscosity and σ_t is the turbulent Schmidt number. In the present approach, both Schmidt numbers in Eqs (5) and (6) were considered to be equal to 1 following Zedler and Street (2001).
The evolution of the mobile bed surface is obtained by the numerical solution of the sediment mass conservation equation, i.e., the Exner equation, expressed as

$$\frac{\partial h}{\partial t} = -\frac{1}{1-n}\left(\frac{\partial q_{x_1}}{\partial x_1} + \frac{\partial q_{x_2}}{\partial x_2}\right) \tag{7}$$

In the above expression, h is the bed level, n = 0.4 is the bed sediment porosity and q_{xi} is the total sediment flux in the horizontal directions x_1 and x_2 respectively, which comprises both bed load, q_b, and suspended load, q_s, transport rates.

$$q_{x_1,x_2} = \left(q_b + q_s\right)_{x_1,x_2} \tag{8}$$

The equation of the morphologic evolution is discretized in time using a 3rd order Adams-Bashforth scheme, applied in both horizontal directions. The spatial gradients are discretized using a 2nd order central difference scheme. An avalanche module is also included in the algorithm in order to avoid development of nonphysical slopes.
It must be stressed that, in the present paper, the morphologic evolution was applied only for the simulations of oscillatory flow over mobile rippled bed, while in the simulations of wave propagation and breaking over a beach of constant slope, the bed was considered to be fixed.

SIMULATION SET-UP

Oscillatory flow over mobile bed

The initial computational domain for the morphological simulations of oscillatory flow over ripples is presented in Fig. 1. The domain is mostly flat, with just a small perturbation in the center, in the shape of a 3D Gaussian hump. In order to imitate a natural coastal environment, periodic boundary conditions were used in both horizontal directions so that the development of ripples is not subjected to space limitations. The vertical dimension of the computational domain was chosen equal to 5 times the orbital motion amplitude so that the development of the boundary layer over the ripples is not suppressed by the upper boundary of the domain. The grid spacing in the horizontal directions, $\Delta x_1/\alpha_o$ and $\Delta x_2/\alpha_o$, is uniform and equal to 0.02, thus, the grid discretization consists of 150 computational nodes. In the vertical direction the grid spacing, $\Delta x_3/\alpha_o$, is varying, with finer resolution near the bottom boundary (=0.005), thus, the grid discretization consists of 300 computational nodes. The computational time-step for the flow simulations was selected to satisfy both the Courant-Friedrichs-Lewy (CFL) and the Viscous Stability Limit criteria, while the computational time-step for the morphological equations was numerically restricted by the morphological CFL condition.
The following approximation for near-bed, wave-induced, oscillatory flow was used:

$$U(t) = U_o\left(\cos\left(\omega t - \pi/2\right) + B\cos\left(2\omega t - \pi/2\right)\right) \tag{9}$$

In Eq. (9), U is the streamwise dimensional velocity of the external flow, $\omega = 2\pi/T$ is the angular wave frequency, T is the wave period, and B is the wave skewness factor. In the present results, the oscillatory flow is driven by a uniform pressure gradient at Reynolds number equal to 23,000 with skewness factor B = 0.176.

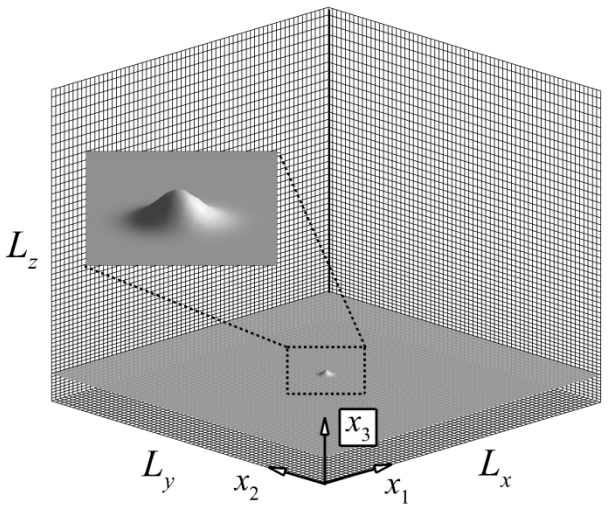

Fig. 1 Schematic of the initial computational domain and the grid (shown every 5th node) used in the morphological simulations of oscillatory flow over ripples.

Wave propagation over a beach of constant slope

In the case of wave propagation over an ideal coast of slope tanβ=1/15, the computational domain is presented in Fig. 2. The length of the computational domain L_x is equal to seven wavelengths. The grid spacing is uniform in all directions. In the horizontal directions it is equal to $\Delta x_1/d_o = \Delta x_2/d_o = 0.1$, while in the vertical direction it is equal to $\Delta x_3/d_o = 0.03$. The incident waves are generated at the left boundary of the computational domain by mimicking the action of a piston-type wavemaker. The waves are initially propagating over an horizontal bed (Fig. 2), so that the waves are fully developed at the time they reach the beginning of the beach. In order to avoid wave reflections from the left boundary of the domain, the method proposed in Jacobsen et al. (2012) was followed for the implementation of a relaxation zone just after the wavemaker. The height of the air layer was selected equal to $3d_o$, so that the upper boundary does not affect the fluid flow field.

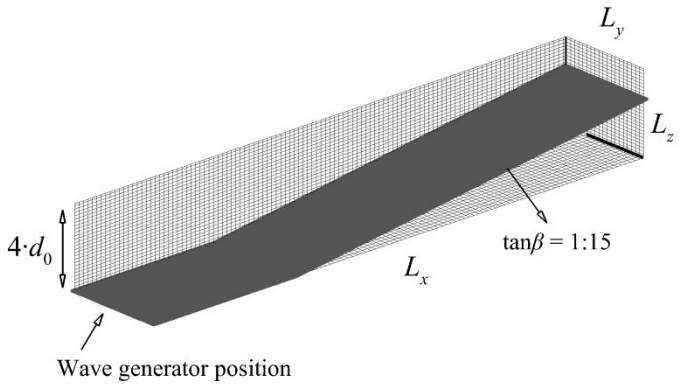

Fig. 2 Schematic of the computational domain and the grid (shown every 5th node) used in the numerical simulations of wave propagation over a constant slope beach.

Parallel implementation

Numerical simulations of coastal flows at high Reynolds numbers are quite demanding it terms of time and computer power consumption. Thus, the use of supercomputers is nowadays mandatory in order to

obtain numerical results in reasonable computational time. In particular, Computational Fluid Dynamics (CFD) algorithms include very fine computational meshes and large numbers of double-precision floating-point operations, which favors the exploitation of modern supercomputing technologies. Due to the extreme computational cost of the present numerical simulations, HPC was used in the specific project. In the morphological simulations of oscillatory flow over ripples, the numerical code has been fully parallelized using a shared memory programming approach (OpenMP). In the case of wave propagation over a beach of constant slope, which is quite more demanding, the algorithm utilizes a distributed memory approach using the MPI protocol, with quite promising results in terms of speedup and acceleration, as presented in Oyarzun et al, 2020. The parallel efficiency of the MPI approach seems to have yet room for improvement, and has the potential to take advantage of modern supercomputing capabilities.

RESULTS AND DISCUSSION

The numerical model has been effectively validated by comparison of flow, sediment transport and free-surface elevation results to experimental and numerical data in the literature. Specifically, such validation comparisons of both laminar and turbulent oscillatory flow, as well as corresponding results of suspended sediment transport have been presented in Dimas and Leftheriotis (2019) for the OpenMP version of the code. The MPI version of the code has been effectively validated for turbulent oscillatory flow in Oyarzun et al. (2020). Finally, validation results of free-surface flow cases for the serial version of the code have been presented in Dimas and Koutrouveli (2019) for wave propagation and breaking over a beach of constant slope tanβ = 1/35.

Morphological evolution of ripples

First, numerical results of the morphological evolution of the bed under hydrodynamic and sediment forcing are presented. All cases correspond to oscillatory flow conditions under the effect of non-breaking waves in the coastal zone. In the specific approach, the shape of the bed form is allowed to change. Every N time steps of coupled flow and suspended sediment simulation, the bed morphology is updated by means of the total sediment transport rate. The value of N is restricted by the CFL condition for the equation of the morphological evolution.

Fig. 3 illustrates an example of ripple creation and propagation from an initially flat bed with a small perturbation in the middle of the computational domain (Fig. 3a) under oscillatory flow conditions. Nielsen (1981) proposed empirical equations to calculate the ripple length, L_r, and the ripple height, h_r, as a function of the mobility parameter, which is defined as:

$$\psi = \frac{U_o^2}{(S-1)gD_g} \tag{9}$$

where S is the specific gravity of the sediment and D_g is the sediment grain diameter. The value of the mobility parameter in the specific simulation is chosen equal to ψ = 50, which corresponds to ripples of length L_r = 0.9a_o according to the equations proposed by Nielsen (1981). Thus, the length of the computational domain in both horizontal directions was set equal to 3.0a_o, in order to capture the development of three consecutive ripples lengths in the streamwise direction (x_1-axis), after equilibrium is reached. It must be stated that the specific value of the streamwise domain length was the smaller one that resulted in the formation of three consequent ripples (after trial and error).

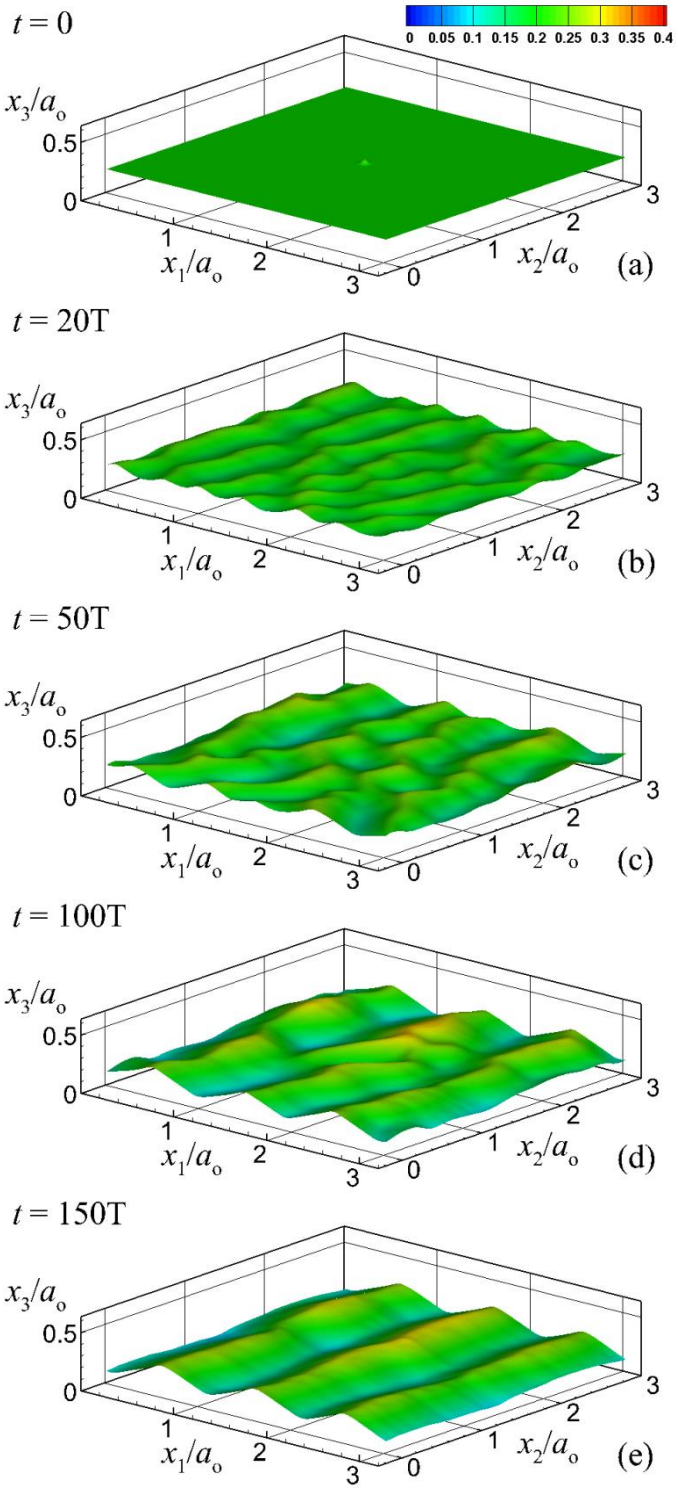

Fig. 3. Ripple creation from a flat bed with an initial perturbation in the middle of the domain. The equilibrium state is reached after 150 wave periods.

The value of a_o/D_g was chosen equal to 500, which is in the range 50-1500 that corresponds to orbital vortex ripples according to Clifton and Dingler (1984). The value of the sediment specific gravity, S = 2.65, corresponds to quartz sand. In the numerical results, the corresponding dimensional values for the flow and sediment parameters are U_o = 0.35

m/s, a_o = 0.076 m, T = 1.357 s, and D_g = 0.151 mm.
After the first 20 wave periods (Fig. 3b), the initial hump has grown in height and has expanded in the spanwise direction (x_2-axis). The initial growth and propagation of the hump is quite rapid, so at that time, the entire computational domain is fully covered with small ripples. At 50 wave periods (Fig. 3c), the geometry of the bed comprises four consecutive ripples lengths, which is close to the predicted final geometry. Then, the morphological evolution seems to decelerate, which is in agreement with the experimental findings in Myrow et al. (2018) who mentioned that the migration rate of ripples is reduced as they grow in size. During the next 50 wave periods, the 2 ripples in the center of the domain are merging into one ripple (Fig. 3d) until the bed finally converges to its equilibrium geometry after 150 wave periods (Fig. 3e). The equilibrium geometry comprises three consequent ripples with lengths of $L_r = 1a_o$ and heights of $h_r = 0.144a_o$ which are in accordance with the equations proposed by Nielsen (1981). After that time, the ripples remain stagnant for the next 300 wave periods.
In Fig. 4, the ripple profile (phase- and spanwise-averaged) is presented at maximum onshore and offshore free-stream velocity for the ripple in the middle of Fig. 3e. It is quite interesting that the ripple crest does not remain still, but it is leaning towards the flow direction during each half wave period. Consequently, stronger and more coherent vortices are produced at flow reversal due to flow separation, than in a similar case of fixed rippled bottom. Noteworthy is the fact that the ripple crest is a little higher at maximum offshore free-stream velocity, due to the external flow skewness. Note that in Fig. 4 the axes are not on the same scale for clarity.

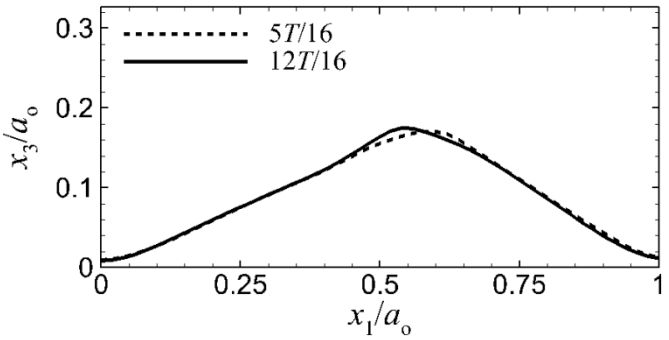

Fig. 4. Phase- and spanwise-averaged ripple profile at maximum onshore and offshore free-stream velocity.

For the bed load, the phase- and spanwise-averaged q_b along x_1 axis is presented in Fig. 5(a) at maximum onshore (5T/16) and offshore (12T/16) free-stream velocity. At the specific phases the bed load transport is active mostly in the vicinity of the ripple crests. This is attributed to the generation of coherent vortices at the lee side of the ripple during each half-cycle which leads to flow separation.
The phase- and spanwise-averaged distribution of q_s along x_1 axis is presented in Fig. 5(b), also at maximum onshore and offshore free-stream velocity. The suspended load transport is active practically over the whole length of the ripples, with maximum positive and negative values at the ripple crests, also due to flow separation.
In the specific case with ψ = 50 and a_o/D_g = 500, the magnitude of bed q_b is comparable to the magnitude of q_s, but the sediment transport is mostly suspended load dominated.

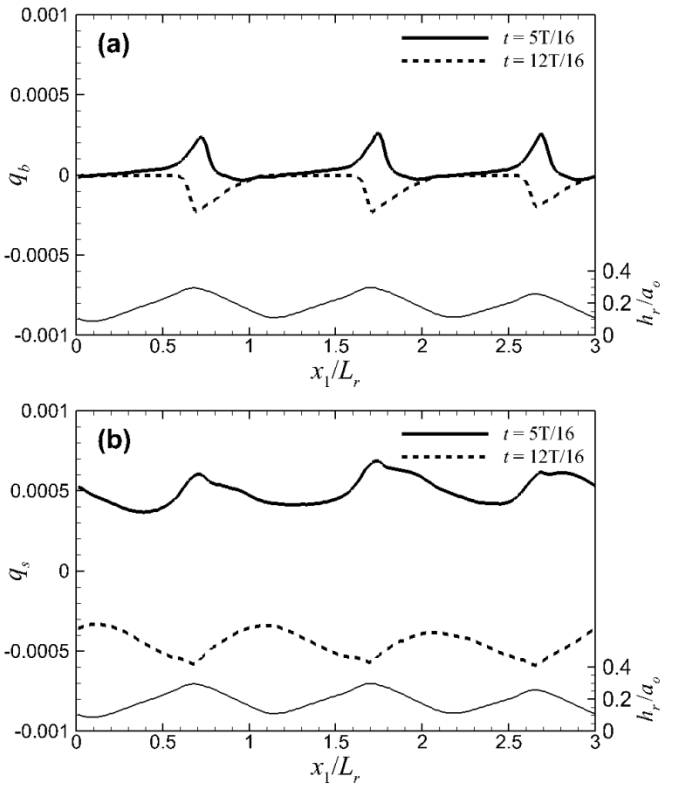

Fig. 5. Phase- and spanwise-averaged bed load (a) and suspended load (b) distribution over three consequent ripple lengths at maximum onshore and offshore free-stream velocity.

Wave propagation over a beach of constant slope

Moreover, numerical results of wave propagation and breaking over a beach of constant slope tanβ = 1/15 are presented. The computational domain of the specific simulations has been presented in Fig. 2. The Reynolds number based on the water depth at the wavemaker is equal to Re_d = 900,000. The characteristics of the incident waves correspond to experimental scale dimensional values of H = 0.06 m for the incident wave height and T_s = 0.92 s for the wave period. The water depth at the wavemaker in dimensional units is equal to d = 0.30 m.
The envelope of the free-surface elevation η during one wave period is presented in Fig. 6, after simulation of 10 wave periods. Wave breaking takes place at $x_1'/d_0 \approx 10$, where x_1' = 0 corresponds to the beginning of the beach slope. After that point, the wave height dissipation is observed in the surf zone.

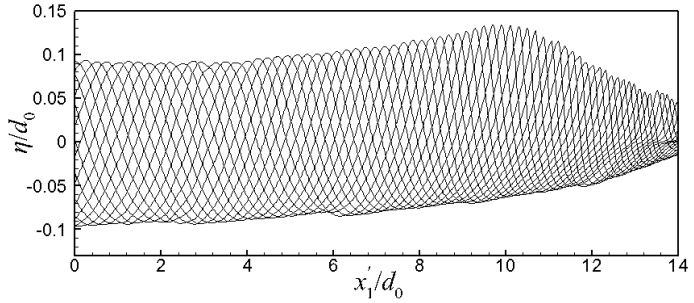

Fig. 6. Envelope of the free surface elevation of waves breaking over a beach of constant slope tanβ = 1/15 (x_1' = 0 is at the beginning of the beach slope).

A typical snapshot of the instantaneous velocity and vorticity fields in the breaking zone at T/16 after breaking is presented in Fig. 7. The level-set method is used for the identification of the interface between fluid and air phase. Positive vorticity (clockwise) is generated in the fluid phase while negative vorticity (counterclockwise) is generated in the air above the breaking face. Similar findings were observed in Dimas and Koutrouveli (2019) for wave propagation and spilling breaking over beaches of constant slope and Larson-type beaches, with tanβ = 1/15 and 1/35. After x_1/d_0 = 19 (Fig. 7), the waves are broken and the undertow is strong, which according to Jacobsen & Fredsøe (2014) leads to large offshore directed suspended flux over a wave period. On the contrary, large orbital velocities are observed at the point of breaking. According to Jacobsen & Fredsøe (2014), these velocities, combined with the small strength of the undertow, lead to large onshore directed suspended flux.

Vorticity generation due to wave propagation and breaking is also presented in three-dimensional form in Fig. 8. Maximum values of vorticity are visible at the level of the free-surface, especially in the regions close to the wave crests. The bed level is illustrated as a black face in the computational domain, while the interface between fluid and air phase is displayed as a continuous isosurface.

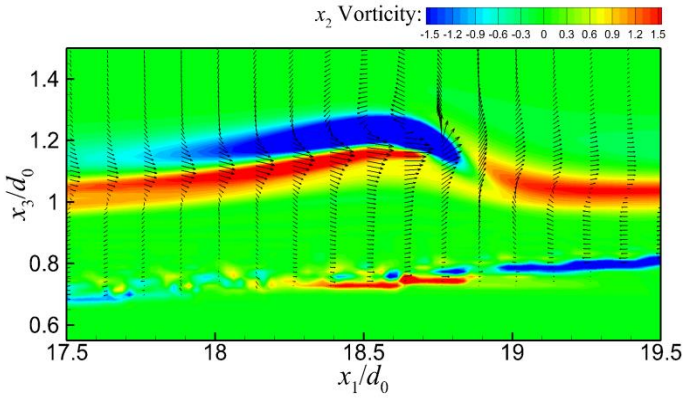

Fig. 7. Snapshot of velocity vectors (every 5 grid points in x_1 axis) and vorticity contours in the breaking zone at T/16 after breaking. Breaking occurs at $x_1/d_0 \approx 18$.

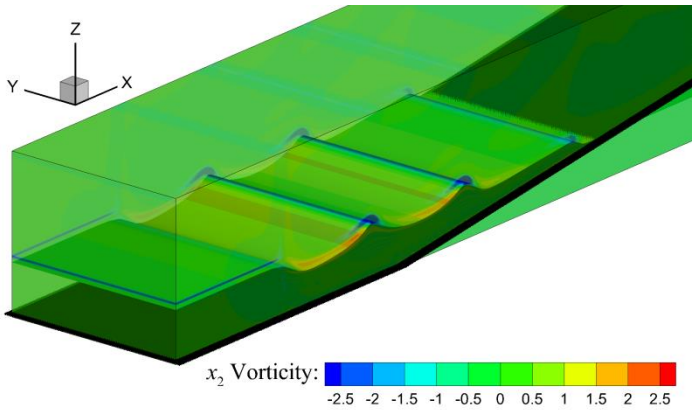

Fig. 8. Vorticity generation due to wave propagation and breaking above a beach of constant slope.

The instantaneous distribution of the suspended sediment concentration is presented in Fig. 9 in the surf zone. The free-surface elevation is illustrated with a straight black line, while the bed level of the beach of constant slope is shown with a dotted black line. It is observed that sediment in suspension has been lifted along the entire length of the surf zone, and at an elevation level of about $0.2 \cdot d_0$. The maximum values of the suspended sediment are located in the breaking zone, due to the higher values of bed shear stress. It must be noted that in Fig. 9 the axes are not on the same scale for clarity.

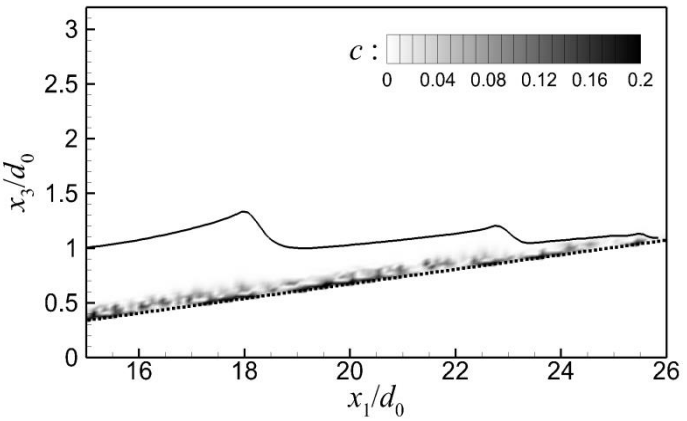

Fig. 9. Contours of suspended sediment concentration in the surf zone. Breaking occurs at $x_1/d_0 \approx 18$.

As already mentioned, in the present numerical simulations of wave propagation and breaking, the bed evolution was not examined as it is still quite demanding in terms of computational resources. This is mostly to the very long characteristic time scale of bed morphology in comparison to the wave period. As a result, the required computational time becomes unreasonably high. A hybrid approach is required, and we pursue, in order to speed-up the computation by taking advantage of the fact that the bed evolution is "slow" in comparison to the "fast" wave hydrodynamics.

CONCLUSIONS

An in-house numerical model has been presented for the numerical simulation of wave propagation, coupled with sediment transport evolution and the corresponding bed morphodynamics. The sediment transport mechanisms of oscillatory flow above a rippled bed have been examined, with numerical results of ripple creation and growth presented at Re = 2.3×10^4, for values of ψ = 50 and a_o/D_g = 500. It is concluded that the ripples end up to equilibrium geometry comprising ripples with lengths and heights with dimensions in accordance with the equations proposed by Nielsen (1981). Sediment loads at maximum onshore and offshore free-stream velocity phases are active mostly close to the ripple crests due to flow separation. The flow for the specific values of ψ and a_o/D_g is slightly suspended load dominated. Moreover, indicative numerical results of wave propagation and breaking are examined over an ideal coast of slope 1/15, accompanied by suspended sediment transport evolution. The numerical model has been fully parallelized using OpenMP in the case of morphological simulation of oscillatory flow over ripples, while in the case of wave propagation the algorithm employs a distributed memory approach using the MPI protocol.

ACKNOWLEDGEMENTS

The present research has been co-financed by Greece and the European Union (European Social Fund- ESF) through the Operational Program "Human Resources Development, Education and Lifelong Learning", in the framework of the "Supporting Postdoctoral Researchers - B cycle" (MIS 5033021) implemented by the State Scholarships Foundation (IKY). This work was supported by computational time granted from the

National Infrastructures for Research and Technology S.A. (GRNET) in the National HPC facility - ARIS - under project ID pr009011_thin – CoastHPC.

REFERENCES

Argyropoulos, CD, and Markatos, NC (2015). "Recent advances on the numerical modelling of turbulent flows", *Appl Math Model*, 39, 693–732.

Clifton, HE and Dingler, JR (1984). "Wave-formed structures and paleoenvironmental reconstruction," *Mar Biol*, 60(1-4) 165–198.

Dally, WR, and Dean, RG (1984). "Suspended Sediment Transport and Beach Profile Evolution," *J Waterw Port Coast Ocean Eng*, 110(1), 15–33.

Dimas, AA, and Chalmoukis, IA (2020). "An adaptation of the immersed boundary method for turbulent flows over three-dimensional coastal/fluvial beds," *Appl Math Model*, 88, 905–915.

Dimas, AA, and Koutrouveli, ThI (2019). "Wave height dissipation and undertow of spilling breakers over beach of varying slope," *J Waterw Port Coast Ocean Eng*, 145(5): 04019016.

Dimas, AA, and Leftheriotis, GA (2019). "Mobility parameter and sand grain size effect on sediment transport over vortex ripples in the orbital regime," *J Geophys Res Earth Surf*, 124 (1), 2–20.

Engelund, F. and Fredsøe, J (1976). "A sediment transport model for straight alluvial channels", *Hydrol Res*, 7(5), 293–306.

Jacobsen, NG, Fuhrman, R, and Fredsøe, J (2012). "A wave generation toolbox for the open-source CFD library: OpenFoam®," *Int J Num Meth Fluids*, 70 (9): 1073–1088.

Jacobsen, NG, and Fredsøe, J (2014). "Formation and development of a breaker bar under regular waves. Part 2: Sediment transport and morphology," *Coast Eng*, 88, 55–68.

Koutrouveli, ThI, and Dimas, AA (2020). "Wave and Hydrodynamic Processes in the Vicinity of a Rubble-Mound, Permeable, Zero-Freeboard Breakwater," *J Mar Sci Eng*, 8(3), 206.

Kraft, S, Yongqi, W, and Oberlack, M (2011). "Large eddy simulation of sediment deformation in a turbulent flow by means of level-set method," *J Hydraul Eng*, 137 (11), 1394–1405.

Leftheriotis, GA, and Dimas, AA (2017). "Large-Eddy Simulation of Oscillatory Flow and Morphodynamics over Ripples," *Procs of the 35th Int Conf on Coastal Eng*, ASCE.

Marieu, V, Bonneton, P, Foster, DL, and Ardhuin, F (2008). "Modeling of vortex ripple morphodynamics," *J Geophys Res*, 113: C09007.

Myrow, PM, Jerolmack, D, and Perron, JT (2018). "Bedform disequilibria: Recent advances and geological applications," *J Sedimentary Res*, 88, 1096–1113.

Nielsen, P (1981). "Dynamics and geometry of wave-generated ripples," *J Geophys Res*, 86(C7), 6467–6472.

Oyarzun, AG, Chalmoukis, IA, Leftheriotis, GA, and Dimas, AA (2020). "A GPU-based algorithm for efficient LES of high Reynolds number flows in heterogeneous CPU/GPU supercomputers", *Appl Math Model*, 85, 141–156.

Sethian, JA, and Smereka, P (2003). "Level Set Methods for Fluid Interfaces," *Annu Rev Fluid Mech*, 35, 341–372.

Smagorinsky, J. (1963) "General circulation experiments with the primitive equations I. The basic experiment" Mon. Weather Rev, 91(3), 99–165.

Van Rijn, LC (1984). "Sediment transport, Part I: Bed load transport," *J Hydraul Eng*, 110(10), 1431–1456.

Zedler, EA, and Street, RL (2001). "Large-eddy simulation of sediment transport: Currents over ripples," *J Hydraul Eng*, 127(6), 442–452.

Zedler, EA, and Street, RL (2006). "Sediment transport over ripples in oscillatory flow," *J Hydraul Eng*, 132(2), 1–14.

\Conf-std\Template-Word-MS-2021